

Faster Swimming Robots Based on In-Plane Prestressed Instability

Zechen Xiong^{1,*}, Liqi Chen², Wenxiong Hao², Yufeng Su², Hod Lipson²

¹*Department of Earth and Environmental Engineering, Columbia University, New York, NY 10027, USA*

²*Department of Mechanical Engineering, Columbia University, New York, NY 10027, USA*

³*School of Mechanical Engineering and Automation, Fuzhou University, Fuzhou 350108, China*

*Correspondence zechex.xiong@columbia.edu

Abstract

Inspired by the snap-through action of a steel hairclip, we propose a design method for in-plane prestressed mechanisms that exhibit biomimetic morphing and high locomotion performance. Compliant bistable flapping mechanisms are fabricated using this method and are mounted on our untethered soft robotic fish. Using this mechanism, we achieve life-like undulation with a Strouhal number (St) of $St = 0.28$ and a velocity of 2.03 body lengths per second (43.6 cm/s), a three-fold improvement over past compliant fish robots. A tethered pneumatic version indicates that this mechanism is compatible with soft actuators. We study the mechanism both computationally and experimentally and suggest that elastic instability may offer a path to overcome the speed challenge of soft and compliant robots.

Summary: A new mechanism that uses in-plane prestress instability to produce large propulsion force and fast speed.

Keywords: soft robotics, in-plane prestressing, compliant mechanism, robotic fish, bistable and multi-stable mechanisms

Main Text

Introduction

Bistable and multi-stable mechanisms are widely found in nature and technology to create rapid and repetitive tasks like hunting, locomoting, and fast deformation (2). These mechanisms achieve large shape transitions in a short amount of time while being both elastic and reversible. Bi-stability is thus useful for programmable materials, morphing structures, and novel applications spanning several orders of size magnitude (3). On the other hand, pre-stressing helps increase the elastic energy released and its release rate in each actuation. Examples of prestressing and multi-stability are common. Many plants can build up elastic energy through osmosis and turgor pressure. A sudden release of this energy can cause rapid movements and plays a critical role in their functions like reproduction and nutrition: the ballistic seed dispersal of *Impatiens* and squirting cucumber after prestressing their seedpods (4); the pollen dispersal of trigger plants (5); the rapid leave closure of the iconic Venus flytrap (6), etc. However, the build-up of turgor pressure takes

large amounts of time and thus cannot support the continuous operation of the prestressed mechanisms.

Interestingly, this prestress-and-snap mechanism is rarely observed in the animal kingdom. Just like animals do not evolve wheels, they cannot grow prestressed and buckling mechanisms due to biological constraints. Prestressing and instability bring about constant static load and repetitive dynamic load, respectively, to the motor systems of animals, and thus can lead to fatal damages. The closest examples, though, would be bird feet that use energy-storing tendons to play zero-powered perching (7) and hummingbird beaks that close fast through snapping due to their being bistable structures (8). Therefore, combining prestressed structures with bistable mechanisms for biomimetic locomotion can be a potential method to not only mimic animals but also see how far the idea can be extended using non-biological materials.

Compared to traditional robotic mechanisms made of rigid links and joints, soft mechanisms are safe, versatile, more bio-mimic, and bio-compatible because of the elastic and compliant materials used, but are intrinsically weaker in force exertion and fast-moving (9, 10). The moduli of soft materials are usually in the order of 10^4 - 10^9 Pa (11). In many cases of soft robots, large blocks of elastomer for self-supporting and end-effectors leads to a comparatively low energy density (11); the widely used fluidic actuation also dissipate too much energy in viscous friction with the tube, especially when the actuation frequency is high (12). To address these problems, about three potential solutions are proposed: larger energy input, higher frequency, and using structural instability. For example, Shepherd et al. (13), Bartlett et al. (14), Tolley et al. (15) and Keithly et al. (16) used explosive actuators to power jumping robots. These robots usually move fast but in a very uncontrollable and unrepeatable pattern and are difficult to repeat frequently. In addition, the soft materials accommodating the explosive impact degenerate rapidly after a few repetitions. Mosadegh et al. (17), Huang et al. (18), Li et al. (19), and Wu et al. (20) designed soft robots with high actuation speed or frequency. However, the highest achievable speed or frequency is severely limited by the low moduli and elastic wave velocities of elastomers, which hinders the use of this method. Tang et al. (21) built a galloping soft robot with a high speed of 2.68 body length per second (BL/s) and a soft swimmer of 0.78 BL/s by utilizing structural instability. Other researches (12, 22, 23) also point to the potential of multi-stable structures leading the next-generation soft robotics. However, presently reported multi-stable structures are still complex in constitution, assembly, and fabrication processes, impeding their development. The method illustrated in this work proposes to create strong bi-stable mechanisms using prestressed 2D materials, which largely decrease the difficulty in design and fabrication.

Using bi-stability for repetitive propulsion

Enlightened by buckling and post-buckling knowledge (24, 25) and the fact that most fast-moving animals in nature need a hard skeleton, we demonstrate in Fig. 1 and movie S1 the geometry and assembly of a hair-clip-like in-plane prestressed mechanism that is fabricated with

materials like metal, plastic, and paper. Even though these materials are high in modulus, the out-of-plane stiffness of the slender ribbons made from them is usually smaller than the membrane stiffness by an order of $10^5 \sim 10^6$, making the ribbons compliant and deformable. By pinning the two extremities of the angled ribbon together with an eyelet rivet, the lateral-torsional buckling of the angled ribbon creates a bi-stable thin-wall spatial surface with non-zero Gaussian curvatures, i.e., a thin-wall dome. The out-of-plane bending angle ψ_l (Fig. 1E) of the ribbon tip ($z = l = L_1 + L_2$) can be calculated from

$$\psi_l \approx \left. \frac{du}{dz} \right|_{z=l} = -\frac{P_{cr}}{EI_\eta} \int_0^l \varphi(l-z) dz, \quad (1)$$

with P_{cr} being the critical load of the lateral-torsional buckling of the angled ribbon, EI_η being the bending stiffness along the η axis, and φ being the angular displacement of the section. Detailed assumptions and derivation can be referred to in the Supplementary Information (SI). The above equation tells the swing amplitude of the HCM during a snap-through. Interestingly, Eq. (1) indicates that ψ_l , a key factor for the kinematic performance of the hair clip mechanism (HCM), is independent of the material modulus E and dimensions like L_1 , L_2 , h , and t , but is only affected by the unitless shape factors θ and $\gamma_s = L_2 / L_1$ (fig. S3), meaning this mechanism is scalable. The estimation of Eq. (1) gives an error smaller than 5% compared to the experimental measurements by the bending sensor in fig. S6.

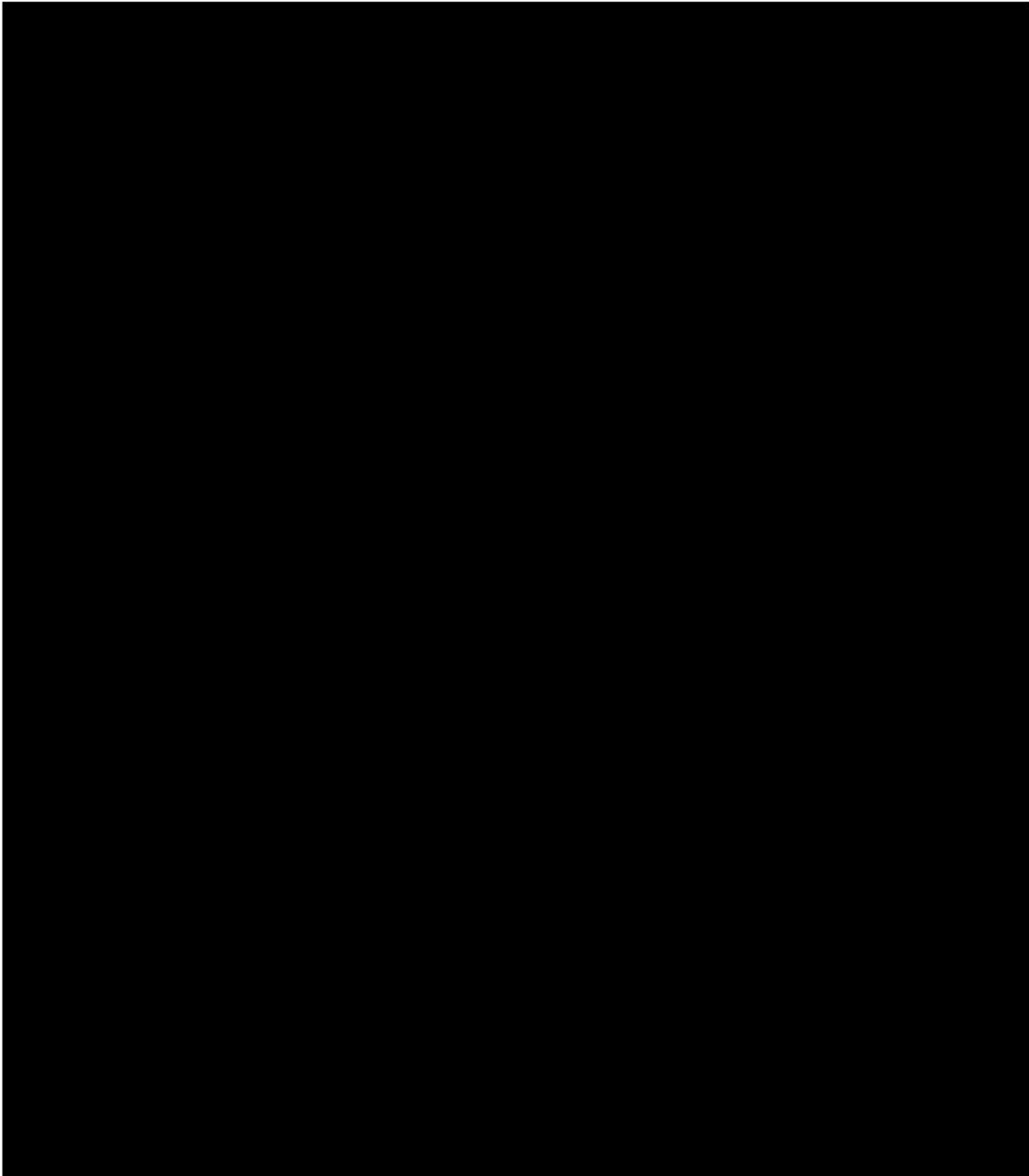
Another key aspect of the HCM is its dynamic feature, which is given by the time scale of the snap-through (26)

$$t_s \approx \frac{l^2}{t\sqrt{E/\rho_s}} \quad (2)$$

where ρ_s is the density of the material. The difference in timescales of HCM snapping is shown using different materials in Fig. 1F and movie S2. A plastic HCM with $\rho_s = 1.2 \text{ g/cm}^3$, thickness $t = 0.381 \text{ mm}$, $E = 1.73 \text{ GPa}$ (SI), and $l = 175 \text{ mm}$ takes about 40 ms to snap and the angular speed is $\sim 4 \times 10^3 \text{ }^\circ/\text{s}$, while a steel HCM with $\rho_s = 7.85 \text{ g/cm}^3$, $t = 0.254 \text{ mm}$, E about 200 GPa, and $l = 175 \text{ mm}$ only takes about 16 ms and have an angular speed of $\sim 14 \times 10^3 \text{ }^\circ/\text{s}$. The theory gives a good estimation. These velocities are comparable to those of the throws of a professional baseball player of $\sim 9000 \text{ }^\circ/\text{s}$ (27) and much faster than the tail beats of fish which is about $100 \sim 1000 \text{ }^\circ/\text{s}$ (28). In the quasi-static energy-storing stage (Fig. 1F), the tip bending angle $|\psi_l|$ of an HCM further increases, and when it snaps, the total energy was released in several to tens of milliseconds, generating fast reverse swinging and small shock waves that result in a clear snap sound (movie S2). Excessive energy is then dissipated through oscillation.

We also noted that the global snap-through of the HCM can be triggered by the inversion of the central segment (denoted by L_1). This means HCMs can be triggered conveniently by

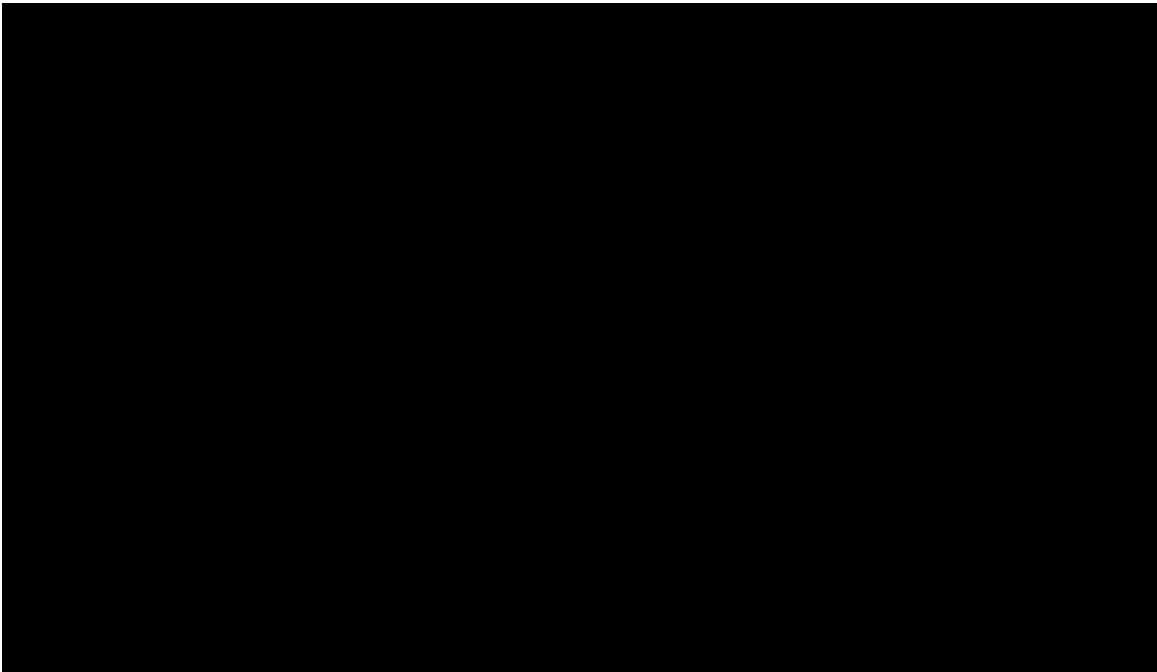
assorted actuation that offers a point displacement at one end, allowing the protruded long props (denoted by L_2) to be used as end effectors of robots or manipulators. This local-global actuation is termed “bend-propagating actuation” in the relevant literature (23). With characteristics like bi-stability, easy actuation and fabrication, and scalability, we believe the in-plane prestressed HCM can be used in domains like origami/kirigami structures (29, 30), deployable devices (24, 31), morphing airfoils (32, 33), etc.



20° and $\gamma_s = 6$). (E) The energy profile and evolution of configuration of the snapping-through of a paper HCM. (F) The dynamics of snapping of a plastic and a metal HCM under a high-speed camera ($\theta = 20^\circ$ and $\gamma_s = 6$).

Untethered motor-driven HCM fish robot

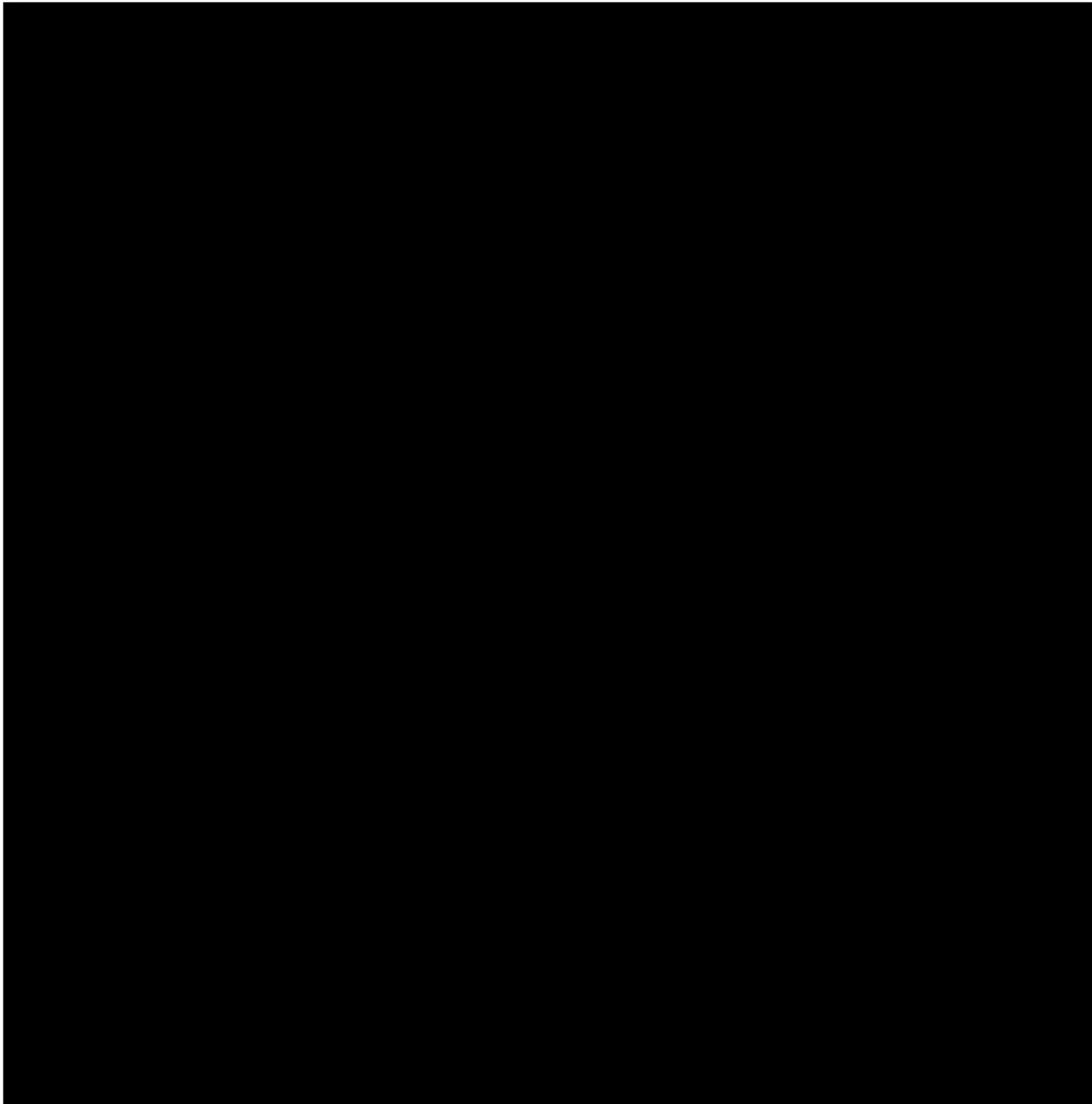
Inspired by the resemblance of the HCM snapping and the undulation of the compliant bodies of fish, we used an HCM in an untethered fish robot to demonstrate its function in aquatic propulsion. The composition of the minimalistic motor-drive fish robot is illustrated in Fig. 2A and fig. S4. The dimensions and weight of the untethered fish robot are length \times width \times height = 21.5cm \times 4.5cm \times 12.0 cm and 125g, respectively. It is made of two major parts: an HCM (coral colored, film thickness $t_1 = 0.762$ mm) with a riveted thinner plastic sheet (blue, film thickness $t_2 = 0.127$ mm) as compliant fish body and fish tail, respectively, and a hollow 3D-printed fish head to guide and balance the motion and to accommodate the Li-ion battery cells, a BLE microcontroller, a servo motor, and wiring stuff to make the robot self-contained. The HCM used in the fish has a shape of $\gamma_s = 2$ and $\theta = -23.5^\circ$, which yields a tip undulation amplitude of $2 \cdot \psi_l = 68^\circ$ according to the theory. The horn of the onboard mini-servo passes through the narrow opening of the waterproof layer made of silicone rubber and moves the center of the HCM ribbon left and right alternately so that the bi-stable HCM can buckle to the opposite sides accordingly (Fig. 2B, 2C, and movie S3). It takes the HCM fish 17 ms and 50 ms to snap in air and underwater, respectively, due to the different drag of the media. The effect of this nonlinear tail beating is discussed in the next section. This repetitive snap-through buckling enables the robot to undulate like a real fish. The blue plastic sheet at the rear of the robot functions as a caudal fin and increases aquatic propulsion. More fast and high-frequency undulation movies of the robot are offered in movie S4.





The equivalent density of the fish robot is set to be slightly smaller than that of water by tuning the weight of the ballast made of silicone rubber and steel balls (fig. S4) so that it can float and receive Bluetooth signals. Besides, the high-density ballast help lower the center of gravity and stabilize the orientation of the fish during its swimming. In Fig. 3A and movie S5, the curvilinear movement is created by adding minor asymmetry to the riveting scheme between the HCM and the caudal fin and is used to provide a longer image sequence for the calculation of swimming speed. Measurements are conducted by comparing the displacement covered in 1s intervals to the length of the fish in the image and it takes the robot about 12.7s to cover the circular path of 554 cm and the speed plot is given in Fig. 3B. With the servo powered by a 7.4V battery pack and a tail beating of 3 Hz, the fish robot can move at an average speed of about 2.03 BL/s (or 43.6 cm/s), which is comparable to the 2~10 BL/s swimming speed of biological fishes (34). This is the fastest untethered soft robotic swimmer, to the best of the authors' knowledge, outperforming the previously reported highest speeds of 0.69 BL/s (19) and 23.5 cm/s (34) by 194% and 86%, respectively (Fig. 3C). Compared to other predecessors, the HCM fish not only excels in velocity per actuation frequency but also triumphs in the simplicity of assembly and fabrication. Interestingly, our fish doesn't scare away aquatic lives but arouses their curiosity sometimes, which indicates its potential for non-disruptive environmental exploring.

The straight swimming of the robot in the aquarium shows its starting stage and an average acceleration of 20.1 cm/s^2 is observed (Fig. 3D, 3E, and movie S3). As expected, the propulsion force increases monotonously w.r.t. flapping frequency of the fish (Fig. 3F, 3G, and movie S6). The nonlinearity of both the speed and force plots is due to the nonlinear relation between drag and speed that $F_D \propto v^2$ (Fig. 3G). These results also indicate that the speed can be further increased.

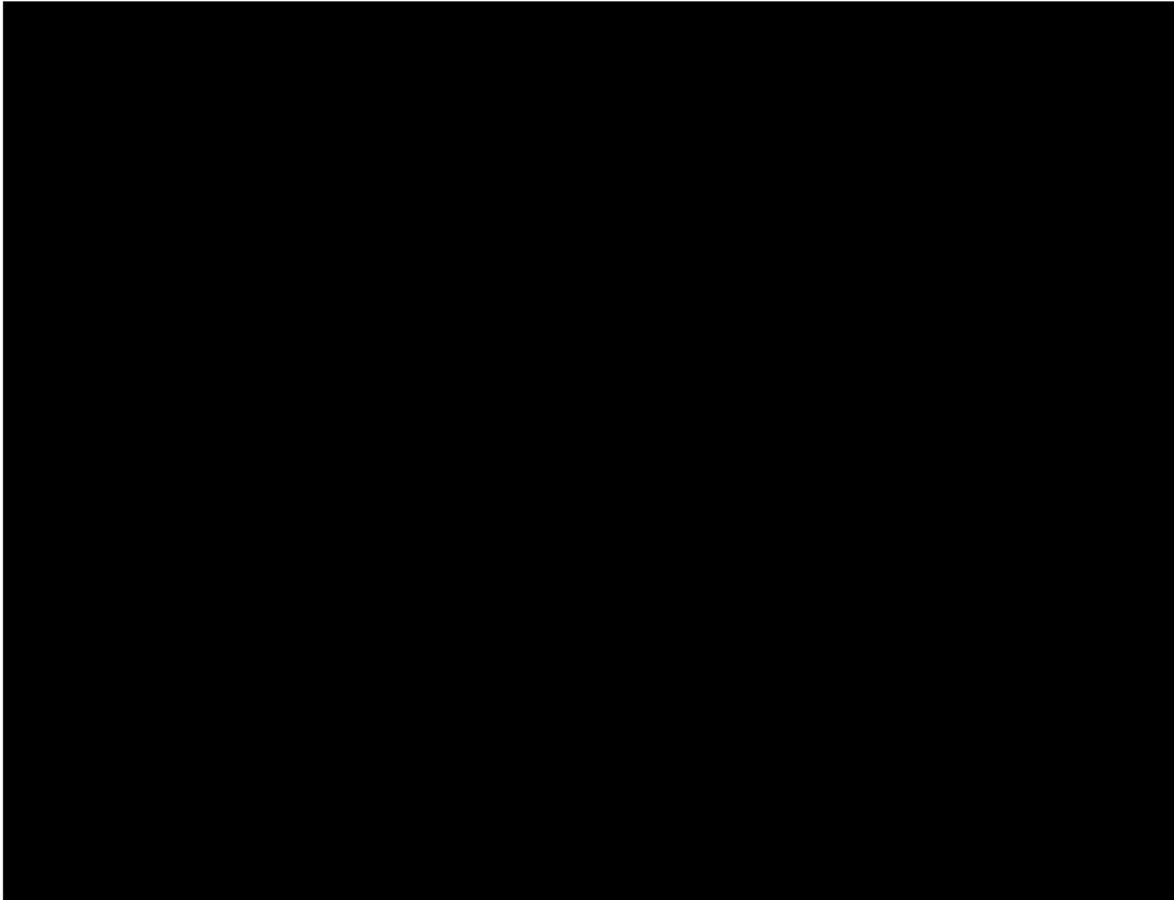


Tethered pneumatic HCM fish robot

To further examine the performance of the HCM and its compatibility with soft actuation methods (10), a pneumatic fish robot is designed and tested in this section (Fig. 4). Using an external energy source and control system, the robot can be made smaller and lighter with dimensions of length \times width \times height = 18.6 cm \times 6.5cm \times 5.2cm and a weight of 42.5 g. It consists of a pneumatic-driven HCM (pink, film thickness $t_1=0.381\text{mm}$) as a fish body, a riveted thinner plastic sheet (grey, film thickness $t_2 = 0.191\text{mm}$) as a fishtail, and a hollow 3D-printed fish head with ballast to guide and balance the motion. The HCM used in the fish has a shape of $\theta = -3^\circ$ and $\gamma_s = 6$, which yield a tip bending angle $\psi_l = 39^\circ$. A pneumatic HCM is built by attaching a

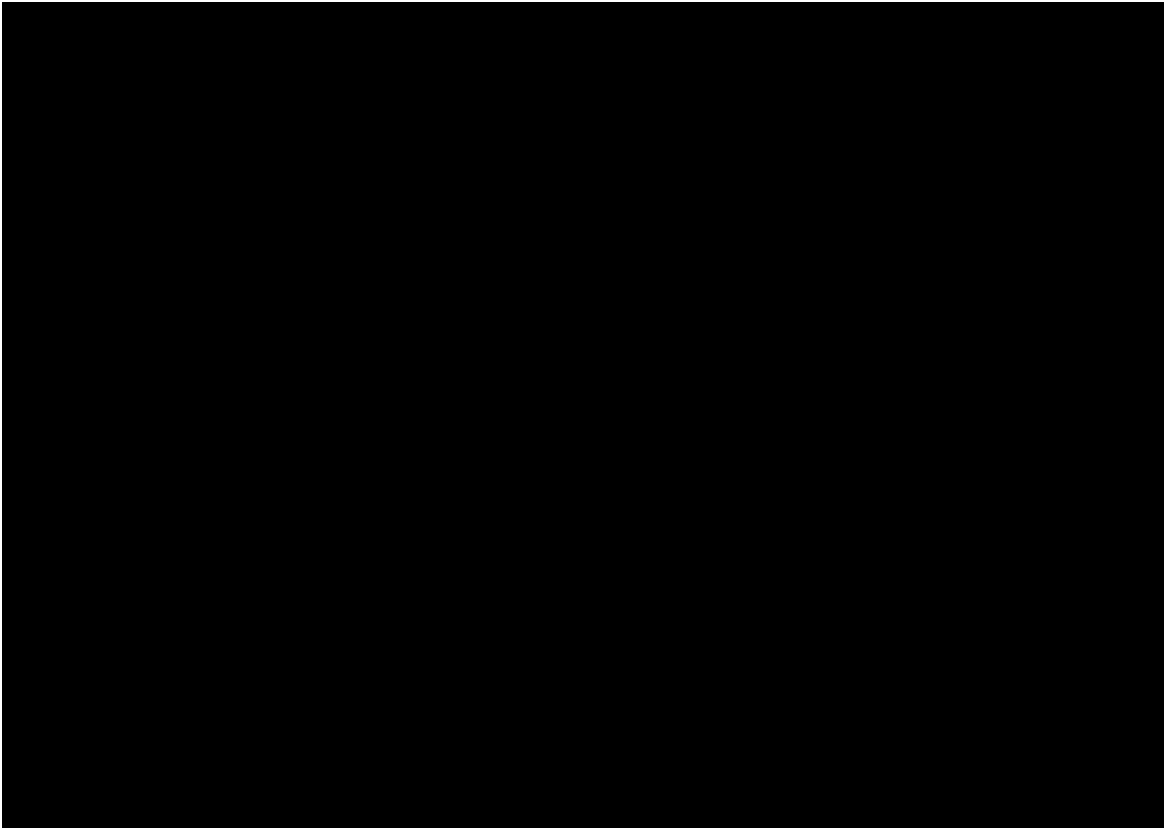
pair of antagonistic soft pneumatic bending units on both sides of the HCM. When gas is pumped into these pneumatic networks (pneu-nets), their bending deformation will snap the mechanism. An alternate actuation of the pneu-nets would enable the HCM to undulate like a biological fish. Fabrication of the pneu-nets is illustrated in SI.

With an actuating pressure of 150 kPa and a frequency of 1.3 Hz (period = 760 ms), the HCM-based bistable pneumatic soft robotic fish swims underwater at an averaged horizontal speed of 1.40 BL/s or 26.54 cm/s (calculated from trigonometry) which is twice as fast as the monostable reference swimmer with the same weight (41.6g) and same actuation conditions (Fig. 4B and movie S7). The reference fish robot, instead of using bistable HCM for the fish body, features a flat and mono-stable plastic sheet with attached pneumatic bending units as actuators. Figure 4C depicts the kinematics of the two pneumatic fish robots, measured from high-fps videos (movie S8). A near-linear actuation swinging is observed in the reference swimmer, while the HCM-driven one shows nonlinear swinging and gains more kinetic energy from each flapping. This is because the drag of fluids is proportional to the squared value of the flapping speed. Even though the HCM fish robot swings with a slightly smaller amplitude than the reference, its angular speed in water is 1200 °/s when its body snaps, about three times that of the reference model of 340 °/s in its linear swings.



The comparison of swimming patterns among a real fish and all these three fish robots can be identified in Fig. 5. A significant feature of the untethered fish robot is its resemblance with the real fish, while the pneumatic and reference models both have obvious deviation. This shows that the bio-fish undulation can be repeated by the HCM method. Despite having a smaller speed than the untethered counterpart, the pneumatic HCM fish has the largest single strike distance among all robots and is almost as good as the real fish, i.e., it has the highest speed per actuation frequency not only among the three robots but also among all previous soft swimmers (fig. S7). Measuring from the sequences, their Strouhal numbers (St) are $St_{\text{untether}} = 3 \times 0.041 / 0.436 = 0.28$, $St_{\text{tether}} = 1.3 \times 0.045 / 0.265 = 0.22$, and $St_{\text{ref}} = 1.3 \times 0.065 / 0.131 = 0.65$, indicating the HCM fish have high propulsive efficiencies.

Contrary to the convention that untethering a soft robotic swimmer usually decreases its swimming capacity (St), having the energy source and control system onboard for an HCM robot increases its speed. This is because the additional weight of the battery and controlling system has little influence on our design since we need weights and ballast to sink the fish anyway, yet the mechanical actuation of a servo is more powerful than soft actuation.



Following the experiments and the energy analysis in the SI, the speed of the HCM-driven fish robots can be increased either by using a larger actuation frequency (Fig. 3G) or by elevating the energy barrier of the HCM to raise the energy released in each snapping (increasing shape

factors θ or decreasing γ_s , shown in Eq. (S17) and fig. S3), which may require higher energy input. For example, a pneumatic HCM with shape factors $\theta = 10^\circ$ and $\gamma_s = 6$ is undulating with an amplitude of $\pm 50^\circ$ and a frequency of 2.5Hz in movie S9, and the actuation pressure required becomes 300 kPa, which is two times the pressure in the 1.3Hz undulation. This also means that energy efficiency is impaired due to larger energy loss in the pneumatic system. The critical pressure needed to snap such pneumatic HCMs is discussed in fig. S9 and the FE simulation of HCM snapping are shown in movie S10.

Conclusion

Harnessing the prestressing and bi-stability of 2D materials opens a new way to morphing mechanisms with enhanced capability and functionality, inspiring applications in diverse fields and scales. Our research not only provides principles for designing and fabricating such hair-clip-inspired mechanisms but also demonstrates the advantages of HCMs as the propulsion method for fish robots. The high force and high speed of the HCM propeller give a record-breaking speed for the untethered compliant swimmer with a significant improvement of 194% compared to conventional ones. The pneumatic HCM fish, on the other hand, indicate the compatibility of HCMs with multiple actuation methods. With an eleven-fold increase in structural rigidity (36), high motion capacity, and energy-storing properties, the HCM combines the functions of skeletons to bear load and muscles to amplify force. This method can be a breach to compete with lives with soft robots and can play a part in the revolution of fast and strong soft robotics.

References and Notes

1. G. K. Taylor, R. L. Nudds, A. L. R. Thomas, Flying and swimming animals cruise at a Strouhal number tuned for high power efficiency. *Nature*. **425**, 707–711 (2003).
2. Y. Chi, Y. Li, Y. Zhao, Y. Hong, Y. Tang, J. Yin, Bistable and Multistable Actuators for Soft Robots: Structures, Materials, and Functionalities. *Advanced Materials*. **34**, 2110384 (2022).
3. N. Hu, R. Burgueño, Buckling-induced smart applications: recent advances and trends. *Smart Mater. Struct.* **24**, 063001 (2015).
4. R. D. Deegan, Finessing the fracture energy barrier in ballistic seed dispersal. *PNAS*. **109**, 5166–5169 (2012).
5. P. E. Taylor, G. Card, J. House, M. H. Dickinson, R. C. Flagan, High-speed pollen release in the white mulberry tree, *Morus alba* L. *Sex Plant Reprod.* **19**, 19–24 (2006).
6. Y. Forterre, J. M. Skotheim, J. Dumais, L. Mahadevan, How the Venus flytrap snaps. *Nature*. **433**, 421–425 (2005).
7. A. Pal, D. Goswami, R. V. Martinez, Elastic Energy Storage Enables Rapid and Programmable Actuation in Soft Machines. *Advanced Functional Materials*. **30**, 1906603 (2020).
8. M. L. Smith, G. M. Yanega, A. Ruina, Elastic instability model of rapid beak closure in hummingbirds. *Journal of Theoretical Biology*. **282**, 41–51 (2011).
9. L. L. Howell, "Compliant Mechanisms" in *21st Century Kinematics*, J. M. McCarthy, Ed. (Springer London, London, 2013; http://link.springer.com/10.1007/978-1-4471-4510-3_7), pp. 189–216.
10. F. Ilievski, A. D. Mazzeo, R. F. Shepherd, X. Chen, G. M. Whitesides, Soft Robotics for Chemists. *Angewandte Chemie International Edition*. **50**, 1890–1895 (2011).
11. D. Rus, M. T. Tolley, Design, fabrication and control of soft robots. *Nature*. **521**, 467–475 (2015).
12. B. Gorissen, D. Melancon, N. Vasios, M. Torbati, K. Bertoldi, Inflatable soft jumper inspired by shell snapping. *Science Robotics*. **5** (2020), doi:10.1126/scirobotics.abb1967.
13. R. F. Shepherd, A. A. Stokes, J. Freake, J. Barber, P. W. Snyder, A. D. Mazzeo, L. Cademartiri, S. A. Morin, G. M. Whitesides, Using Explosions to Power a Soft Robot. *Angewandte Chemie International Edition*. **52**, 2892–2896 (2013).
14. N. W. Bartlett, M. T. Tolley, J. T. B. Overvelde, J. C. Weaver, B. Mosadegh, K. Bertoldi, G. M. Whitesides, R. J. Wood, A 3D-printed, functionally graded soft robot powered by combustion. *Science*. **349**, 161–165 (2015).

15. M. T. Tolley, R. F. Shepherd, M. Karpelson, N. W. Bartlett, K. C. Galloway, M. Wehner, R. Nunes, G. M. Whitesides, R. J. Wood, "An untethered jumping soft robot" in *2014 IEEE/RSJ International Conference on Intelligent Robots and Systems* (2014), pp. 561–566.
16. D. Keithly, J. Whitehead, A. Voinea, D. Horna, S. Hollenberg, M. Peck, J. Pikul, R. F. Shepherd, A cephalopod-inspired combustion powered hydro-jet engine using soft actuators. *Extreme Mechanics Letters*. **20**, 1–8 (2018).
17. B. Mosadegh, P. Polygerinos, C. Keplinger, S. Wennstedt, R. F. Shepherd, U. Gupta, J. Shim, K. Bertoldi, C. J. Walsh, G. M. Whitesides, Pneumatic Networks for Soft Robotics that Actuate Rapidly. *Advanced Functional Materials*. **24**, 2163–2170 (2014).
18. X. Huang, K. Kumar, M. K. Jawed, A. M. Nasab, Z. Ye, W. Shan, C. Majidi, Chasing biomimetic locomotion speeds: Creating untethered soft robots with shape memory alloy actuators. *Science Robotics*. **3** (2018), doi:10.1126/scirobotics.aau7557.
19. T. Li, G. Li, Y. Liang, T. Cheng, J. Dai, X. Yang, B. Liu, Z. Zeng, Z. Huang, Y. Luo, T. Xie, W. Yang, Fast-moving soft electronic fish. *Science Advances*. **3**, e1602045 (2017).
20. Y. Wu, J. K. Yim, J. Liang, Z. Shao, M. Qi, J. Zhong, Z. Luo, X. Yan, M. Zhang, X. Wang, R. S. Fearing, R. J. Full, L. Lin, Insect-scale fast moving and ultrarobust soft robot. *Science Robotics*. **4** (2019), doi:10.1126/scirobotics.aax1594.
21. Y. Tang, Y. Chi, J. Sun, T.-H. Huang, O. H. Maghsoudi, A. Spence, J. Zhao, H. Su, J. Yin, Leveraging elastic instabilities for amplified performance: Spine-inspired high-speed and high-force soft robots. *Sci. Adv.* **6**, eaaz6912 (2020).
22. J. Sun, B. Tighe, J. Zhao, "Tuning the Energy Landscape of Soft Robots for Fast and Strong Motion" in *2020 IEEE International Conference on Robotics and Automation (ICRA)* (2020), pp. 10082–10088.
23. S.-W. Kim, J.-S. Koh, J.-G. Lee, J. Ryu, M. Cho, K.-J. Cho, Flytrap-inspired robot using structurally integrated actuation based on bistability and a developable surface. *Bioinspir. Biomim.* **9**, 036004 (2014).
24. Z. Xiong, H. Xiao, X. Chen, Fractal-inspired soft deployable structure: a theoretical study. *Soft Matter*. **17**, 4834–4841 (2021).
25. Y. Zhang, Y. Jiao, J. Wu, Y. Ma, X. Feng, Configurations evolution of a buckled ribbon in response to out-of-plane loading. *Extreme Mechanics Letters*. **34**, 100604 (2020).
26. M. Gomez, D. E. Moulton, D. Vella, Critical slowing down in purely elastic ‘snap-through’ instabilities. *Nature Phys.* **13**, 142–145 (2017).
27. N. T. Roach, M. Venkadesan, M. J. Rainbow, D. E. Lieberman, Elastic energy storage in the shoulder and the evolution of high-speed throwing in Homo. *Nature*. **498**, 483–486 (2013).

28. *Fish Swimming* (<https://link.springer.com/book/10.1007/978-94-011-1580-3>).
29. Y. Yang, K. Vella, D. P. Holmes, Grasping with kirigami shells. *Science Robotics*. **6**, eabd6426 (2021).
30. Y. Tang, G. Lin, S. Yang, Y. K. Yi, R. D. Kamien, J. Yin, Programmable Kiri-Kirigami Metamaterials. *Advanced Materials*. **29**, 1604262 (2017).
31. W. Wang, H. Rodrigue, S.-H. Ahn, Deployable Soft Composite Structures. *Scientific Reports*. **6**, 20869 (2016).
32. S. Daynes, K. D. Potter, P. M. Weaver, Bistable prestressed buckled laminates. *Composites Science and Technology*. **68**, 3431–3437 (2008).
33. S. Daynes, P. M. Weaver, Stiffness tailoring using prestress in adaptive composite structures. *Composite Structures*. **106**, 282–287 (2013).
34. R. K. Katzschmann, J. DelPreto, R. MacCurdy, D. Rus, Exploration of underwater life with an acoustically controlled soft robotic fish. *Science Robotics*. **3** (2018), doi:10.1126/scirobotics.aar3449.
35. P. W. Webb, J. M. Skadsen, Strike tactics of *Esox*. *Can. J. Zool.* **58**, 1462–1469 (1980).
36. Z. Xiong, Y. Su, H. Lipson, Fast Untethered Soft Robotic Crawler with Elastic Instability (2022), , doi:10.48550/arXiv.2210.02352.
37. F. G. Serchi, A. Arienti, C. Laschi, Biomimetic Vortex Propulsion: Toward the New Paradigm of Soft Unmanned Underwater Vehicles. *IEEE/ASME Transactions on Mechatronics*. **18**, 484–493 (2013).
38. S.-H. Song, M.-S. Kim, H. Rodrigue, J.-Y. Lee, J.-E. Shim, M.-C. Kim, W.-S. Chu, S.-H. Ahn, Turtle mimetic soft robot with two swimming gaits. *Bioinspir Biomim*. **11**, 036010 (2016).
39. M. D. Bartlett, N. Kazem, M. J. Powell-Palm, X. Huang, W. Sun, J. A. Malen, C. Majidi, High thermal conductivity in soft elastomers with elongated liquid metal inclusions. *PNAS*. **114**, 2143–2148 (2017).
40. H. Jin, E. Dong, G. Alici, S. Mao, X. Min, C. Liu, K. H. Low, J. Yang, A starfish robot based on soft and smart modular structure (SMS) actuated by SMA wires. *Bioinspir Biomim*. **11**, 056012 (2016).
41. M. Sfakiotakis, A. Kazakidi, A. Chatzidaki, T. Evdaimon, D. P. Tsakiris, "Multi-arm robotic swimming with octopus-inspired compliant web" in *2014 IEEE/RSJ International Conference on Intelligent Robots and Systems* (2014), pp. 302–308.

Acknowledgments

We especially thank Yichao Tang for their help with the experiments, Jiefeng Sun for the simulation suggestion, and all colleagues for the inspiring discussions. **Funding:** This work was supported by the Earth Engineering Center and the Center for Advanced Materials for Energy and Environment at Columbia University. **Author contributions:** Z. X. conceived the presented idea, developed the theory, built the simulation, and wrote the manuscript. Z. X., L. C., W. H., and Y. S. designed and carried out the experiments. H. L. supervised the project. **Competing interests:** There are no conflicts of interest to declare. **Data and materials availability:** All data are available in the manuscript or the supplementary materials.

Supplementary Materials for:
Faster Swimming Robots Based on In-Plane
Prestressed Instability

Zechen Xiong^{1,*}, Liqi Chen², Wenxiong Hao², Yufeng Su², Hod Lipson²

¹*Department of Earth and Environmental Engineering, Columbia University, New York, NY 10027, USA*

²*Department of Mechanical Engineering, Columbia University, New York, NY 10027, USA*

³*School of Mechanical Engineering and Automation, Fuzhou University, Fuzhou 350108, China*

**Correspondence zechen.xiong@columbia.edu*

The PDF file includes:

supplementary text
fig. S1 to S9
Captions for movies S1 to S10

Other Supplementary Material:

movies S1 to S10

Methods

Derivation of the theory

The assembly and function of the hair-clip mechanism (HCM) are illustrated in Fig. 1 of the main text. To derive the mathematic solutions, the variables are defined in fig. S1: displacement components u , v , and φ are measured on centroid C of an arbitrary section mn along x , y , and z axes (undeformed coordinates), respectively, with signs following the directions of axes and right-hand rule; the ξ , η , and ζ axes (deformed coordinates) are drawn through the deformed centroid C' of the section mn , coinciding with the principal axes of the deformed configuration. Following the small deflection theory and Euler's beam theory, and assuming the angled ribbon to be a straight cantilever beam of a rectangular section (fig. S1A), the mathematical model of the assembly process can be given by the following equations (33):

$$EI_{\xi} \frac{d^2v}{dz^2} + P(l-z) = 0 \quad (S1)$$

$$EI_{\eta} \frac{d^2u}{dz^2} + P\varphi(l-z) = 0 \quad (S2)$$

$$C \frac{d\varphi}{dz} + P(l-z) \frac{du}{dz} - P(u_1 - u) = 0 \quad (S3)$$

in which EI_i is the bending stiffness of the axis, $l = L_1 + L_2$ is the half-length of the strip, $C = GJ = hb^3G/3$ is the torsional rigidity of the thin rectangular section mn , u_1 is the horizontal deflection at $z = l$, and G is the shear modulus. Differentiating Eq. (S3) w.r.t z and plugging in Eq. (S2) yield

$$C \frac{d^2\varphi}{dz^2} + \frac{P^2(l-z)^2}{EI_{\eta}} \varphi = 0 \quad (S4)$$

The general solution of Eq. (S4) can be analytically given as

$$\varphi = \sqrt{s} \left[A_1 J_{1/4} \left(\frac{\beta_1}{2} s^2 \right) + A_2 J_{-1/4} \left(\frac{\beta_1}{2} s^2 \right) \right] \quad (S5)$$

where $s = l - z$, $J_{1/4}$ and $J_{-1/4}$ represent Bessel functions of the first kind of order $1/4$ and $-1/4$, respectively, and the notation

$$\beta_1 = \sqrt{\frac{P^2}{EI_{\eta} C}}. \quad (S6)$$

Due to the symmetry of the ribbon and small deflection assumption, integration constant $A_2 = 0$ can be inferred from the boundary condition

$$\varphi|_{s=0} = 0. \quad (S7)$$

Thus, the general solution of Eq. (S1)-(S3) can be described by

$$\varphi = \sqrt{s} A_1 J_{1/4} \left(\frac{\beta_1}{2} s^2 \right) \quad (S8)$$

with A_1 being a non-zero integration constant. This means the ribbon will buckle approximately in the shape of a Bessel function. Similarly, another boundary condition of the beam is

$$\varphi|_{s=l} = 0 \quad (S9)$$

Due to the lack of lateral support on the beams, the lowest root of the Bessel function should be used when combining Eq. (S8) and (S9), which yields

$$\frac{\beta_1}{2} l^2 = 2.7809 \quad (S10)$$

Plugging in Eq. (S3), the critical load of the lateral-torsional buckling is

$$P_{cr} = \frac{5.5618}{l^2} \cdot \sqrt{EI_\eta C} \quad (S11)$$

To determine the value of A_1 and then φ , an additional equation, usually the energy conservation equation, is included. The energy equation dictates that the total elastic strain energy of the structure must equal the work done by the external load. Ignoring the membrane strain energy, we have

$$U = \frac{1}{2} \int_0^l \left[\frac{M_\eta^2}{EI_\eta} + GJ \left(\frac{d\varphi}{dz} \right)^2 \right] dz \quad (S12)$$

$$= \frac{1}{2} \int_0^l \left[P_{cr}^2 (l-z)^2 \sin^2 \varphi / EI_\eta + GJ \left(\frac{d\varphi}{dz} \right)^2 \right] dz$$

$$T = P_{cr} \cdot L_2 \left(\sin^{-1} \frac{1}{\gamma_s} + \theta \right) \quad (S13)$$

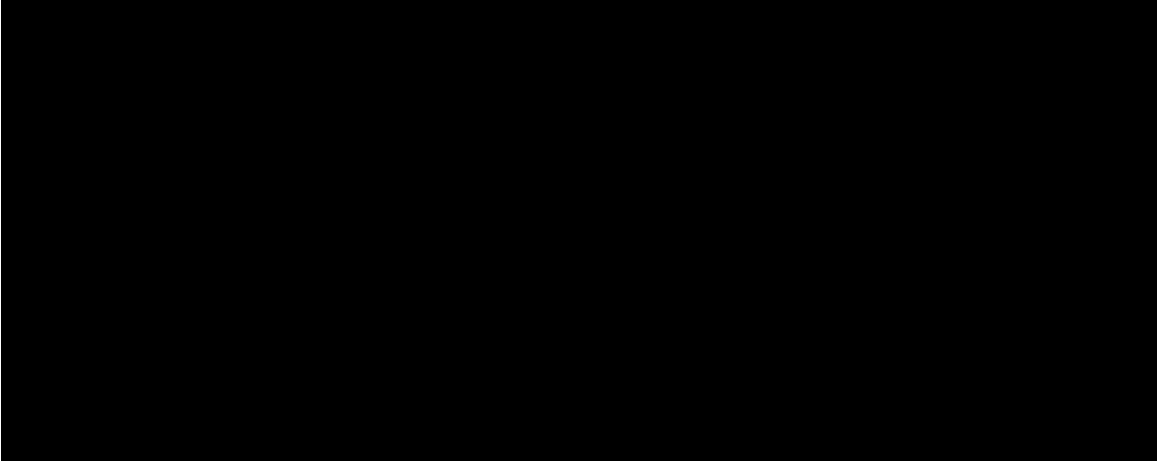
and

$$U = T \quad (S14)$$

in which U is the elastic strain energy, M_η is the moment on the beam along axis η , and T is the external work done by P_{cr} . The typical value of A_1 is $0.09 \sim 0.10$, depending on the value of $\gamma_s = L_2/L_1$ and θ (Fig. 1). The analytical expression of φ is then calculated from Eq. (S8). Finally, by plugging Eq. (S8) into Eq. (S2), the out-of-plane bending angle ψ of the section mn can be calculated from

$$\psi \approx \frac{du}{dz} = -\frac{P_{cr}}{EI_\eta} \int_0^z \varphi(l-z) dz \quad (\text{S16})$$

The verification of Eq. (S16) or its derivation Eq. (1) in the main text is done by comparing it to a corresponding finite element (FE) simulation illustrated in the Fig. S2, S3, and movie S10.



The derivation of the energy profile needs additional assumptions because the energy-storing process is path-dependent. Assuming the snapping of an HCM is similar to that of an axially compressed beam as in fig. S3D, the dimensionless energy barrier of the bi-states of the HCM can also be derived from the above inference (SI), which is

$$\bar{U}_{barr} \approx 3\bar{U} \Big|_{\psi_l = -\psi_{eq} \text{ or } \psi_{eq}} = 3P_{cr} \cdot L_2 \left(\sin^{-1} \frac{1}{\gamma_s} + \theta \right) \quad (\text{S17})$$

To calculate the energy barrier of the bi-stable HCM, we assume the assembled HCM is perfectly symmetric and the local maximum and minima of the tip bending angle are

$$\psi_l \Big|_{\frac{dU}{d\psi_l} = 0} = -\psi_{eq}, 0, \psi_{eq}, \quad (\text{S18})$$

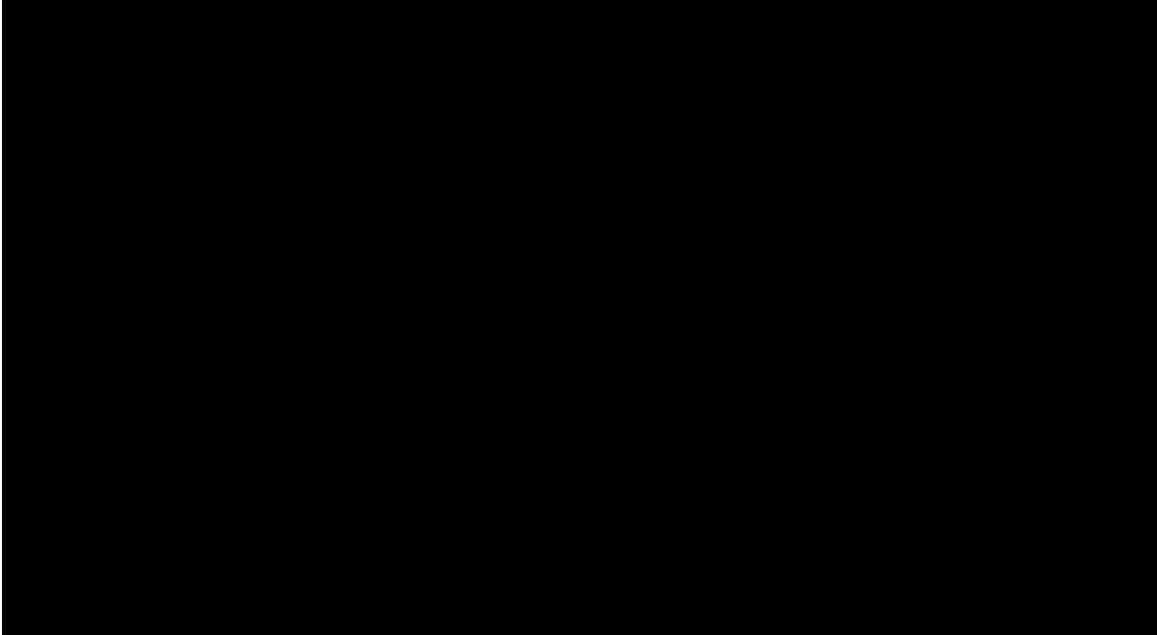
where ψ_{eq} is the equilibrium tip angle after assembly (Fig. 1), and thus energy barrier

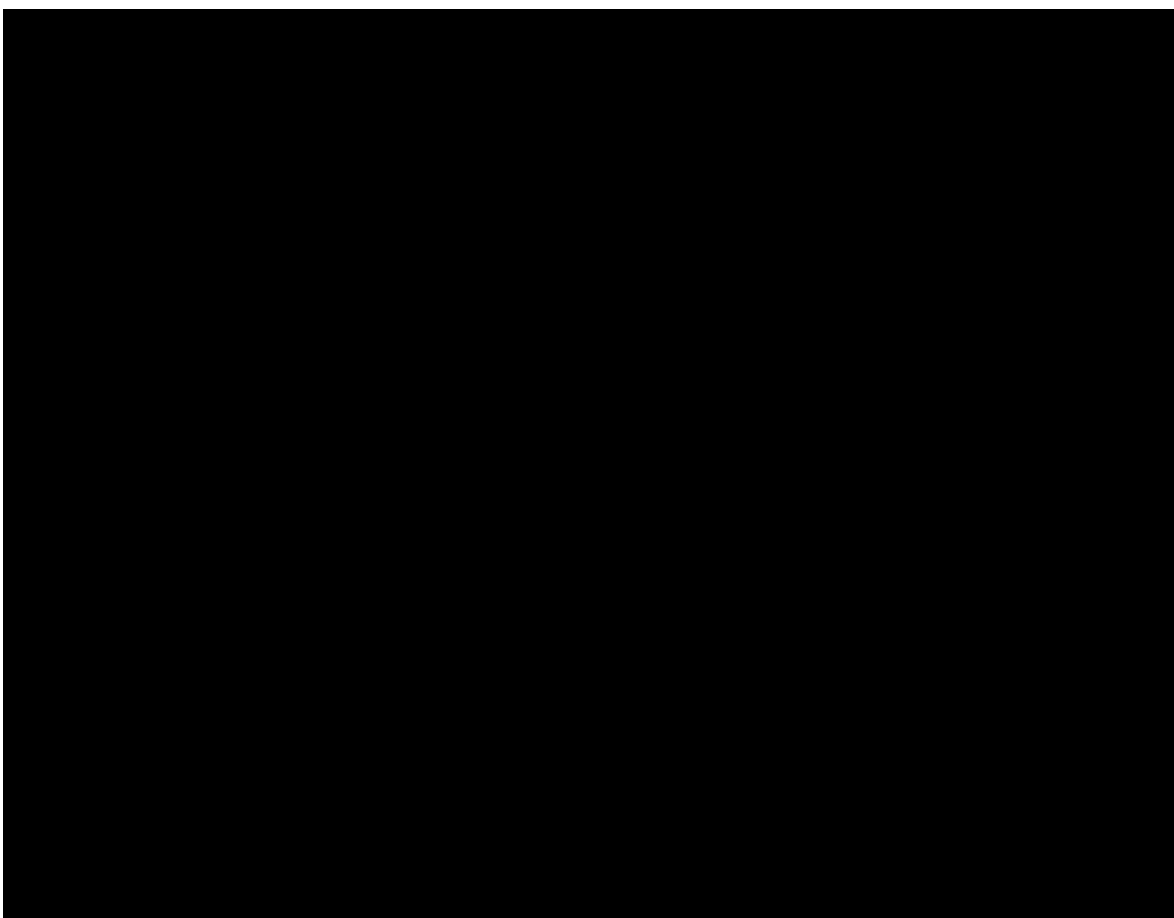
$$U_{barr} = U \Big|_{\psi_l = 0} - U \Big|_{\psi_l = -\psi_{eq} \text{ or } \psi_{eq}} \quad (\text{S19})$$

Verification of the theory

According to the theory, the HCM ribbons buckle in the shape of a Bessel function when it is assembled, as in Eq. (S8). We reproduced this process in the finite element (FE) software of ABAQUS/Standard for an HCM with shape factor $\theta = 10^\circ$, $\gamma_s = 6$, and other parameters $h / L_1 = 15 \text{ mm} / 12.5 \text{ mm}$ and $t / L_1 = 0.381 \text{ mm} / 12.5 \text{ mm}$. The simulation uses 756 shell elements S4R and the material is assumed to be linear elastic with a Young's modulus (E) of 2 GPa and Poisson ratio (ν) of 0.3 (Fig. 1B). And the theoretic solution of the rotation angle φ is calculated using Matlab. The comparison in fig. S2 shows a fair consistency between these two methods with a maximum error of 7 % appearing at the vertex C . However, this theory is still qualitative because of the multiple assumptions used like small deflection, equivalent straight beam, etc.

The comparisons of other derivations of the theory with FE and experiment results are provided in fig. S3. The accuracy of Eq. (S16) is also discussed in the main text. Counterintuitively, tip bending angle ψ_l decreases with an increasing dimensionless prop length γ_s . The verification of the energy barrier is through finding the difference between the maximum and minimum of the strain energy profile when HCM snaps in the FE simulation. One of the simulated cases of HCM snap-through is given in the movie S10. In fig. 3E, an error within 10% is observed. Again, the energy gap \bar{U}_{barr} also depends merely on the parameters θ and γ_s , indicating the scale-free nature of HCM. For example, increasing the thickness t by twofold doesn't change ψ_l and \bar{U}_{barr} , yet leads to an eight-fold rise in U_{barr} . These scalable features can inspire novel designs of morphing structures, metamaterial, and soft robots in both macro- and milli-scales.



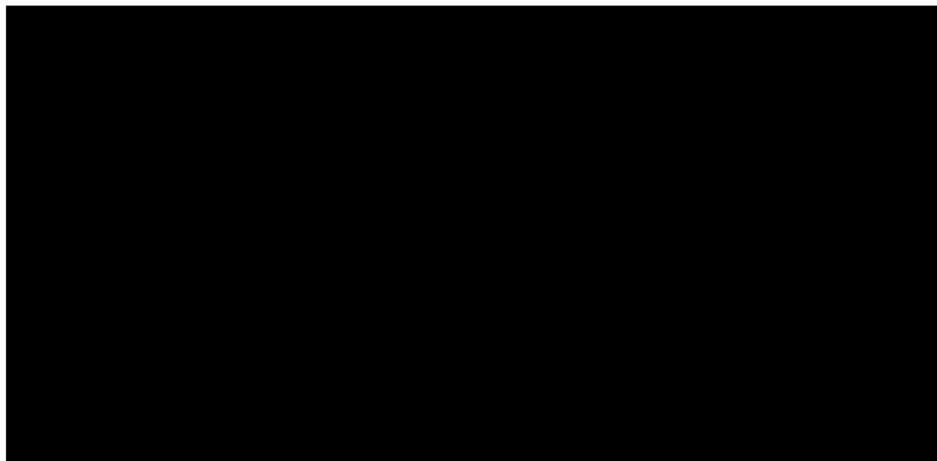


Fabrication of the fish robots

Both the fish heads from the motor-driven fish and the pneumatic fish are modeled in Solidworks and 3D printed. The plastic HCM ribbons are laser-cut (using Thunder Laser Nova51) from color-coded shims (McMaster-Carr, 9536K) and metal HCM ribbons are water jetted from stainless steel shim stock sets (McMaster-Carr, 93005K). In the assembly of these HCMs, the extremities of HCMs are pin-locked using press-fit rivets (McMaster-Carr, 97362A) (fig. S4, Fig. 2 and 4). The pneumatic soft bending units are fabricated using the 3D-printed molds (Ultimaker S3, PLA) and cast with Dragon Skin 20 (Smooth-On Inc.), as shown in fig. S5. Plastic glue (Loctite Super Glue) is used to bond the cured silicone rubber bending units to the plastic shims.



Bending angles of assembled HCMs are measured using a 1-Axis Soft Flex Sensor (Bend Labs Inc.) that is connected to the microcontroller of SparkFun Pro nRF52840 Mini (fig. S6). A broader comparison of robotic speed and frequency of our research to other works is shown in fig. S7. The hollow circles in the figure denote tethered swimmers and solid circles denote untethered ones.



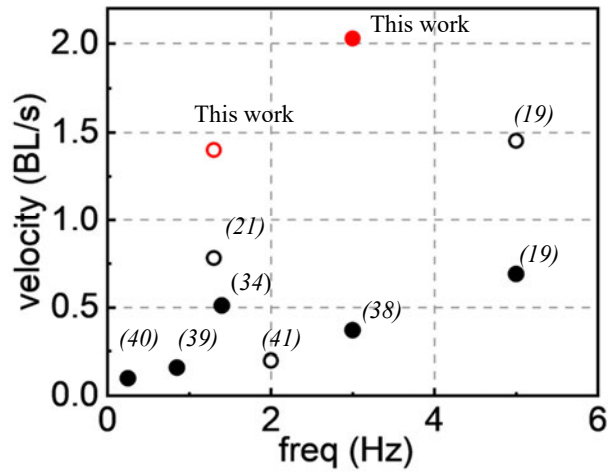
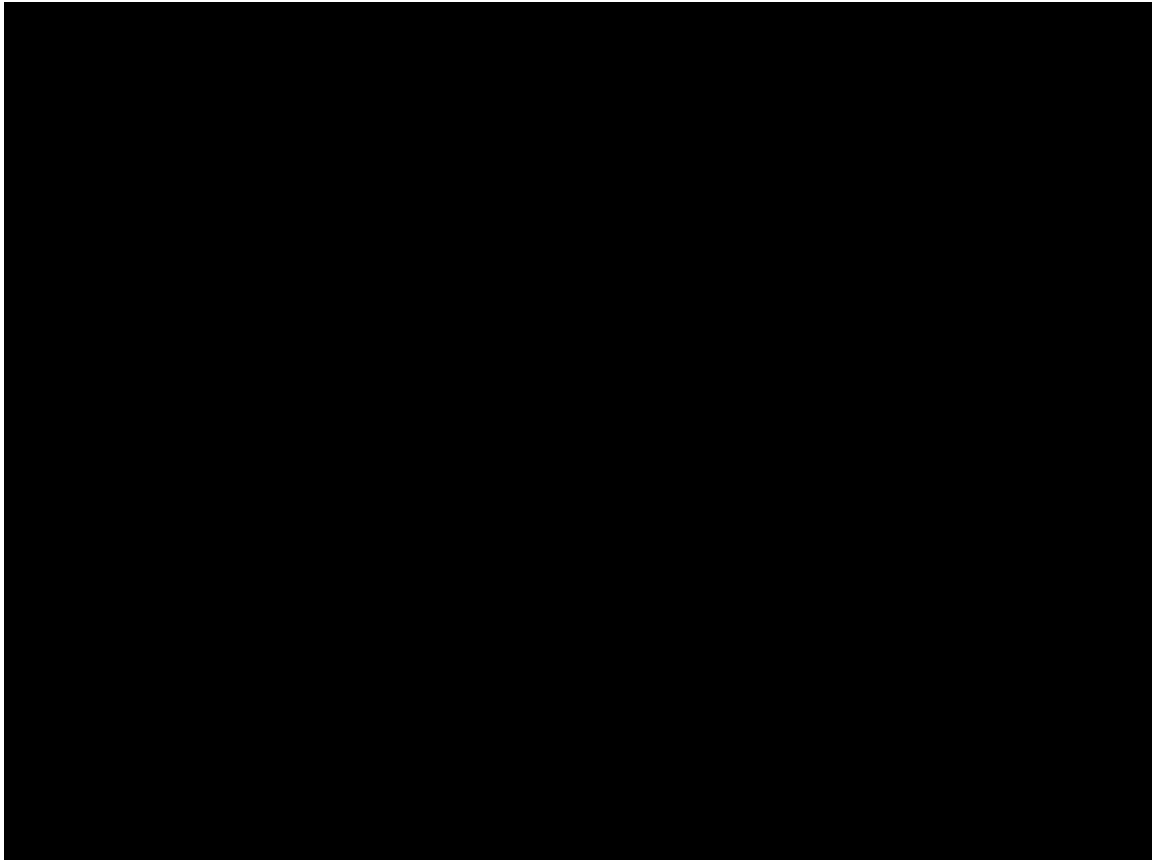


fig. S7 Comparison of swimming velocity w.r.t actuation frequency among the HCA-driven and various reported soft robotic swimmers. The hollow circles in the figure denote tethered swimmers and solid circles denote untethered swimmers. The red-colored symbols are fishes in this work.

Material properties

According to the theory illustrated in Fig. 1 and 2, the Young's moduli of the materials of an HCM have a critical influence on its mechanical features. While the modulus of the steel can be estimated to be 200 GPa, the moduli of the PETG color-coded plastic sheet (McMaster-Carr, 9536K) and the silicone rubber (Smooth-On Inc., Dragon Skin 10) are measured via a tensile machine (SUNS, UTM4000), following the guidance of ASTM D882 and ASTM E8/E8M, respectively. Five PETG samples are laser-cut (Thunder Laser Nova51) and three silicone rubber samples are cast from 3D-printed molds (Ultimaker S3, PLA plastic). The process and results are shown in fig. S5. Assuming linear elasticity, the moduli of the PETG plastic sheets (averaged from 5 samples) and Dragon Skin 20 silicone rubber (averaged from 3 samples) are 1.73 Gpa and 885 kPa, respectively.



Pneumatic Actuation of the HCM

By gluing pneumatic bending units to the surface of an HCM, we create a bi-stable fishtail mechanism whose snap-through buckling can be triggered by pumping air into the bending pneu-nets. The pressure needed for the onset of HCM snapping, which is called critical pressure, is measured with the setup in fig. S9. A quasi-static pressurizing scheme is applied until snap-through, and the critical pressure is measured on HCMs with different values of shape factor θ yet constant $\gamma_s = 6$. The curve is divided into two linear segments. The linear relation is because the energy barrier of the HCM is proportional to shape factor θ , according to the theoretical expression of the energy barrier in Eq. (6). The slope of the curve is smaller when $\theta > 0$ than when $\theta < 0$. This is because the ridges of the soft pneu-nets (fig. S2) will contact and interfere with each other at the rest state when $\theta > 0$ and make the snap-through of the pneumatic HCM easier.



Movie captions:

movie S1. The assembly of PETG and steel HCMs. The thickness and shape factors of the PETG plastic HCM ribbon are $t = 0.381\text{mm}$, $\theta = 20^\circ$, and $\gamma_s = L_2 / L_1 = 6$, while those of the metal HCM are $t = 0.152\text{mm}$, $\theta = 10^\circ$, and $\gamma_s = 6$

movie S2. The slo-mo (0.125x) demonstration of the snapping of plastic and metal HCMs. The PETG plastic HCM snap in ~ 40 ms and the metal HCM in $\sim 16\text{ms}$

movie S3. The undulation of the untethered fish robot in the air and underwater. The HCM used in the robot has shape factors $\theta = -23.5^\circ$, and $\gamma_s = 2$. An average acceleration of 20.1 cm/s^2 is observed in the starting stage of the robotic straight swimming in the aquarium.

movie S4. The high-frequency undulation of the motor-driven fish. The shape factors of the fish HCM are $\theta = -23.5^\circ$ and $\gamma_s = 2$, and the frequencies of the swinging are 2.5, 3.0, 3.5, and 4.0 Hz.

movie S5. The circular swimming of the motor-driven HCM fish in a lake. The shape factors of the fish HCM are $\theta = -23.5^\circ$ and $\gamma_s = 2$, and the undulation frequency is 3 Hz, yielding an average speed of 2.03 BL/s (43.6 cm/s).

movie S6. The setup for the propulsion measurement of the fish. The fish is tied to a pulley system at the tip of the fishtail, and a spring force gauge is filmed with a camera to determine the instantaneous force readings.

movie S7. The Comparison of real-time swimming of the HCM-driven fish robot and its conventional soft counterpart. The pneumatic actuation system pressurizes at 150 kPa and 1.3 Hz for both of the tests. The HCM used in the robot has shape factors $\theta = -3^\circ$, and $\gamma_s = 6$.

movie S8. The Comparison of slo-mo swimming of the HCM-driven fish robot and its conventional soft counterpart. The movie is filmed at 240 fps.

movie S9. The high-frequency real-time swinging of the pneumatic HCM fishtail. The HCM has shape factors $\theta = 10^\circ$, and $\gamma_s = 6$. The pneumatic actuation system pressurizes at $\sim 300\text{kPa}$ and 2.5Hz.

movie S10. The simulated process of the assembly and actuation of the HCM and pneumatic HCM. The dimensions for both models are $t = 0.381\text{ mm}$, $\theta = 10^\circ$, and $\gamma_s = 6$.